ACS Catalysis

Research Article

pubs.acs.org/acscatalysis

Trimodal Porous Hierarchical SSZ-13 Zeolite with Improved Catalytic Performance in the Methanol-to-Olefins Reaction

Xiaochun Zhu,[†] Jan P. Hofmann,[†] Brahim Mezari,[†] Nikolay Kosinov,[†] Leilei Wu,[†] Qingyun Qian,[‡] Bert M. Weckhuysen,[‡] Shunsuke Asahina,[§] Javier Ruiz-Martínez,[‡] and Emiel J. M. Hensen*[,†]

[†]Inorganic Materials Chemistry, Schuit Institute of Catalysis, Department of Chemical Engineering and Chemistry, Eindhoven University of Technology, P.O. Box 513, 5600 MB, Eindhoven, The Netherlands

[‡]Inorganic Chemistry and Catalysis, Debye Institute for Nanomaterials Science, Utrecht University, Universiteitsweg 99, 3584 CG Utrecht, The Netherlands

[§]JEOL Ltd., Akishima, Tokyo 196-8558, Japan

Supporting Information

ABSTRACT: Chabazite zeolites with trimodal porosity (native micropores of the CHA framework, an additional network of larger micropores of ~0.5 nm, and mesopores) were synthesized by adding diquarternary ammonium-type surfactant C_{22-4-4} cations and fluoride anions in the synthesis of SSZ-13 zeolite. The hierarchical SSZ-13 zeolites are fully crystalline and exhibit similar acidity as bulk SSZ-13 zeolite. The increased diffusion rate in the hierarchical SSZ-13, proven by uptake experiments of bulky molecules and selective staining by thiophene oligomers, resulted in much slower catalyst deactivation in the methanol-to-olefins (MTO) reaction. Confocal fluorescent images of spent hierarchical SSZ-13 zeolites reveal homogeneous distribution of carbonaceous deposits, indicating that the micropore space has been completely utilized during the MTO reaction.

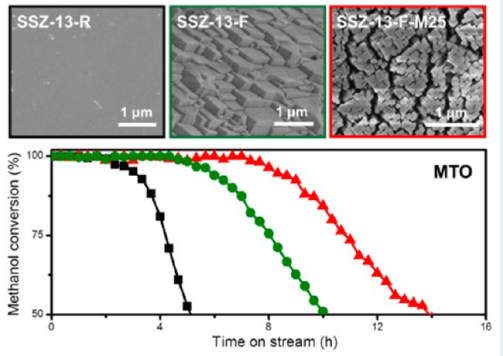

KEYWORDS: *zeolite, SSZ-13, porosity, deactivation, carbonaceous deposits, methanol-to-olefins*

INTRODUCTION

The methanol-to-olefins (MTO) reaction has rapidly become an important practical technology for converting methanol to valuable light olefins.[1−5] In industrial practice, H-SAPO-34, which is a microporous silicoaluminophosphate with the chabazite (CHA) framework topology, is the preferred catalyst.[6,7] CHA contains large cavities with a size of 6.7 Å × 10.9 Å connected by small pore openings of 3.8 Å. Dahl and Kolboe were the first to suggest that methanol conversion to olefins and aromatics involves hydrocarbon pool species that built up during acid-catalyzed reactions of methanol in zeolites and related microporous materials.[8,9] There is compelling evidence that polymethylated benzenes are involved in converting methanol into light olefins in H-SAPO-34 and other small-pore zeolites.[10] It is assumed that these methylbenzenes slowly age with time on stream into multiring aromatics, which cause blocking of the micropores and, in this way, catalyst deactivation.[4,11]

H-SSZ-13 is the aluminosilicate analogue of H-SAPO-34. The stronger acidity of the bridging hydroxyl groups in H-SSZ-13[12] results in faster deactivation during methanol conversion due to the rapid buildup of carbonaceous deposits in the internal voids of the zeolite crystals, which will limit the effectiveness factor.[13−16] Several groups have attempted to introduce intracrystalline mesopores in zeolite particles to lower the deactivation rate. Typical approaches for mesopore generation in zeolites, such as alkaline leaching and steaming, did not lead to the expected performance increase when applied to H-SSZ-13.[13,17] Wu et al. synthesized mesoporous H-SSZ-13 by using, in addition to the structure-directing agent TMAdaOH, a diquaternary ammonium-type surfactant $[C_{22}H_{45}-N^+(CH_3)_2-C_4H_8-N^+(CH_3)_2-C_4H_9]Br_2$ ($C_{22-4-4}\cdot Br_2$ for brevity) in the synthesis gel.[18,19] Related diquaternary ammonium surfactants have earlier been used to synthesize ZSM-5 zeolite nanosheets.[20] An important aspect of the work of Wu et al. was the combination of two templates, one for structure direction of the zeolite and the other to generate sufficient intracrystalline mesopores. At an optimized $C_{22-4-4}\cdot Br_2$/TMAdaOH ratio, the lifetime of mesoporous H-SSZ-13 in the MTO reaction was three times higher than that of bulk H-SSZ-13.

Usually, zeolites are synthesized in alkaline media (high pH) under hydrothermal conditions. The use of fluoride media near neutrality to synthesize zeolites was a significant development in the 1980s. This allowed for a number of new zeolite structures, mostly high-silica zeolites, to be obtained.[21,22] There have been only very few works that discuss the influence of fluoride on zeolite synthesis carried out at high pH.[23−27] It has

Received: November 4, 2015
Revised: February 8, 2016
Published: February 26, 2016

DOI: 10.1021/acscatal.5b02480
ACS Catal. 2016, 6, 2163−2177

for instance been reported that the crystal morphology of BEA zeolite changes when the pH of the fluoride-containing gel is increased from near-neutral to basic.[25]

Recently, we reported a new approach to obtain bimodal microporous zeolite H-SSZ-13. The use of fluoride in the alkaline synthesis of H-SSZ-13 zeolite results in fine-grained zeolite crystals that contain an additional system of micropores.[28] These micropores are larger than the pore apertures inherent to the CHA micropore network and, as such, result in increased accessibility of the zeolite crystal and a greatly increased lifetime in the MTO reaction. In the present work, we further investigate this approach and explore its combination with the mesoporogen $C_{22-4-4}{\cdot}Br_2$ to arrive at H-SSZ-13 zeolite with trimodal porosity. The resulting trimodal porous hierarchical H-SSZ-13 zeolites display the highest performance in the MTO reaction in terms of the total methanol conversion capacity among H-SSZ-13 zeolites described in the literature so far. The structural, textural, and acidic properties of these new materials were scrutinized in detail by XRD, electron microscopy, Ar physisorption, NMR, and IR spectroscopy. Visible light microspectroscopy and confocal fluorescence microscopy were employed to identify the nature and location of carbonaceous deposits during the MTO reaction.

EXPERIMENTAL SECTION

Synthesis of Mesoporogen $C_{22-4-4}{\cdot}Br_2$. First, 4.1 g (0.01 mol) of 1-bromodocosane (Aldrich, 96%) was dissolved in 20 mL of toluene (Biosolve, 99.5%) and added dropwise to a 20 mL solution of 10.3 g (0.07 mol) of *N,N,N′,N′*-tetramethyl-1,4-butanediamine (Aldrich, 98%) in acetonitrile (Biosolve, 99.8%). The solution was refluxed in an oil bath at 70 °C for 12 h. After cooling to room temperature, the solution was filtered and washed with diethyl ether. The resulting product $[C_{22}H_{45}{-}N^+(CH_3)_2{-}C_4H_8{-}N(CH_3)_2]Br$ was dried in a vacuum oven at 50 °C. Then, 3.7 g (0.007 mol) of $[C_{22}H_{45}{-}N^+(CH_3)_2{-}C_4H_8{-}N(CH_3)_2]Br$ and 1.96 g (0.014 mol) of 1-bromobutane (Aldrich, 98%) were dissolved in 110 mL of acetonitrile and stirred under reflux at 70 °C for 12 h. The resulting solution was cooled, filtered, washed with diethyl ether, and dried in a vacuum oven at 50 °C. The product was $[C_{22}H_{45}{-}N^+(CH_3)_2{-}C_4H_8{-}N^+(CH_3)_2{-}C_4H_9]Br_2$, which will be denoted as $C_{22-4-4}{\cdot}Br_2$.

Synthesis of Zeolites. H-SSZ-13 zeolite was synthesized according to a published procedure.[19] In a typical synthesis of H-SSZ-13, Ludox AS 40 (Aldrich, 40 wt %), aluminum hydroxide (Aldrich, reagent grade), sodium hydroxide (EMSURE, 50 wt %), *N,N,N*-trimethyl-1-adamantammonium hydroxide (TMAdaOH, SACHEM Inc., 25 wt %), and demineralized water were mixed to obtain a gel with a molar composition of 20 TMAdaOH:7.5 Na_2O:2.5 Al_2O_3:100 SiO_2:4400 H_2O. The resulting gel was stirred at room temperature for 2 h and then transferred into a 45 mL Teflon-lined steel autoclave. The gel was crystallized statically at 160 °C for 6 days. The resulting reference zeolite is denoted as SSZ-13-R. Another SSZ-13 zeolite was synthesized by adding sodium fluoride (EMSURE, ≥99.5%) to the above recipe of SSZ-13-R to give the gel composition 20 TMAdaOH:7.5 Na_2O:10 NaF:2.5 Al_2O_3:100 SiO_2:4400 H_2O. The final gel was crystallized statically at 160 °C for 10 days; the obtained zeolite is denoted as SSZ-13-F.

A set of mesoporous SSZ-13 zeolites, denoted as SSZ-13-F-M*x* in which a fraction of TMAdaOH replaced by $C_{22-4-4}{\cdot}Br_2$ (*x* represents the fraction of TMAdaOH replaced). The total N content of the synthesis gel was kept constant. $C_{22-4-4}{\cdot}Br_2$ was added to the gel for SSZ-13-F synthesis, and the mixture was stirred for 2 h. The final gel was transferred into a Teflon-lined autoclave and crystallized statically at 160 °C for 12 days. Another mesoporous SSZ-13 zeolite was synthesized following the recipe for SSZ-13-F-M*x* without addition of NaF to give a gel with the composition 19 TMAdaOH:7.5 Na_2O:2.5 Al_2O_3:100 SiO_2:0.5 $C_{22-4-4}{\cdot}Br_2$:4400 H_2O. This gel was crystallized statically at 160 °C for 12 days; the obtained zeolite is denoted as SSZ-13-R-M5. After crystallization, the zeolite products were filtered, washed with demineralized water, and dried at 110 °C. The zeolites were calcined at 550 °C for 10 h under flowing air and ion-exchanged three times with 1.0 M NH_4NO_3 solutions followed by calcination at 550 °C for 4 h to obtain their proton forms.

Catalyst Characterization. X-ray diffraction patterns were recorded using a Bruker D4 Endeavor diffractometer using Cu Kα radiation in the 2θ range of 5−60°. Elemental analyses were carried out by ICP-OES on a Spectro Ciros CCD ICP optical emission spectrometer with axial plasma viewing. The surface area and porosity of the zeolites were determined by Ar physisorption at −186 °C on a Micromeritics ASAP 2020 instrument in static mode. The samples were outgassed at 400 °C for 8 h prior to the sorption measurements. The Langmuir adsorption isotherm model was used to determine the total surface area in the p/p_0 range between 0.05 and 0.20. The mesopore volume and mesopore size distribution were calculated from the adsorption branch of the isotherm by the Barrett−Joyner−Halenda (BJH) method. The micropore volume was determined by the *t*-plot method, and the micropore diameter was calculated by the NLDFT model. The model for Ar adsorption on oxides in cylindrical pores at −186 °C was used without regularization.

Scanning electron microscopy (SEM) images were taken using an FEI Quanta 200F scanning electron microscope at an accelerating voltage of 3−5 kV. The zeolites were coated with gold prior to analysis. We also employed low-voltage high-resolution scanning electron microscopy (LV-HRSEM). A high-purity carbon stub was used as sample support. The carbon stub was cleaned by ultrasonication in ethanol followed by heating in a vacuum before mounting the sample. The SSZ-13-F-M50 sample was picked on a cotton ball swab and dropped onto the stub and then heated in a vacuum oven for 10 min at 200 °C. Afterwards, the sample was cleaned by an Ar ion cleaner placed in the load-lock chamber of the LV-HRSEM instrument at 300 V for 10 min. All images were taken with the in-column detector of a JEOL JSM-7800F GBSH.

The carbonaceous deposits formed during the MTO reaction were analyzed by thermogravimetric analysis (TGA) on a TGA/DSC 1 STAR system from Mettler Toledo. For this purpose, the temperature of the sample was increased to 850 °C at a rate of 5 °C min^{-1} in flowing artificial air (50 mL min^{-1} 20 vol % O_2 in He). The weight loss between 300 and 600 °C was considered as the total carbonaceous deposit content. To evaluate differences in diffusion in the zeolites, the adsorptions of methanol, ethylene, propylene, *n*-butanol, and *i*-butanol were investigated in the same TGA apparatus. The samples were first dehydrated at 550 °C and then exposed to the gaseous adsorbent at 30 °C. For the liquid adsorbents, a He flow was led through a thermostated saturator. The gaseous adsorbents were mixed with a He flow. The partial pressures of the adsorbents were 2.8 mbar for methanol, 6.9 mbar for *n*-butanol, 4.3 mbar for *i*-butanol, and 47 mbar for ethylene and propylene.

DOI: 10.1021/acscatal.5b02480
ACS Catal. 2016, 6, 2163−2177

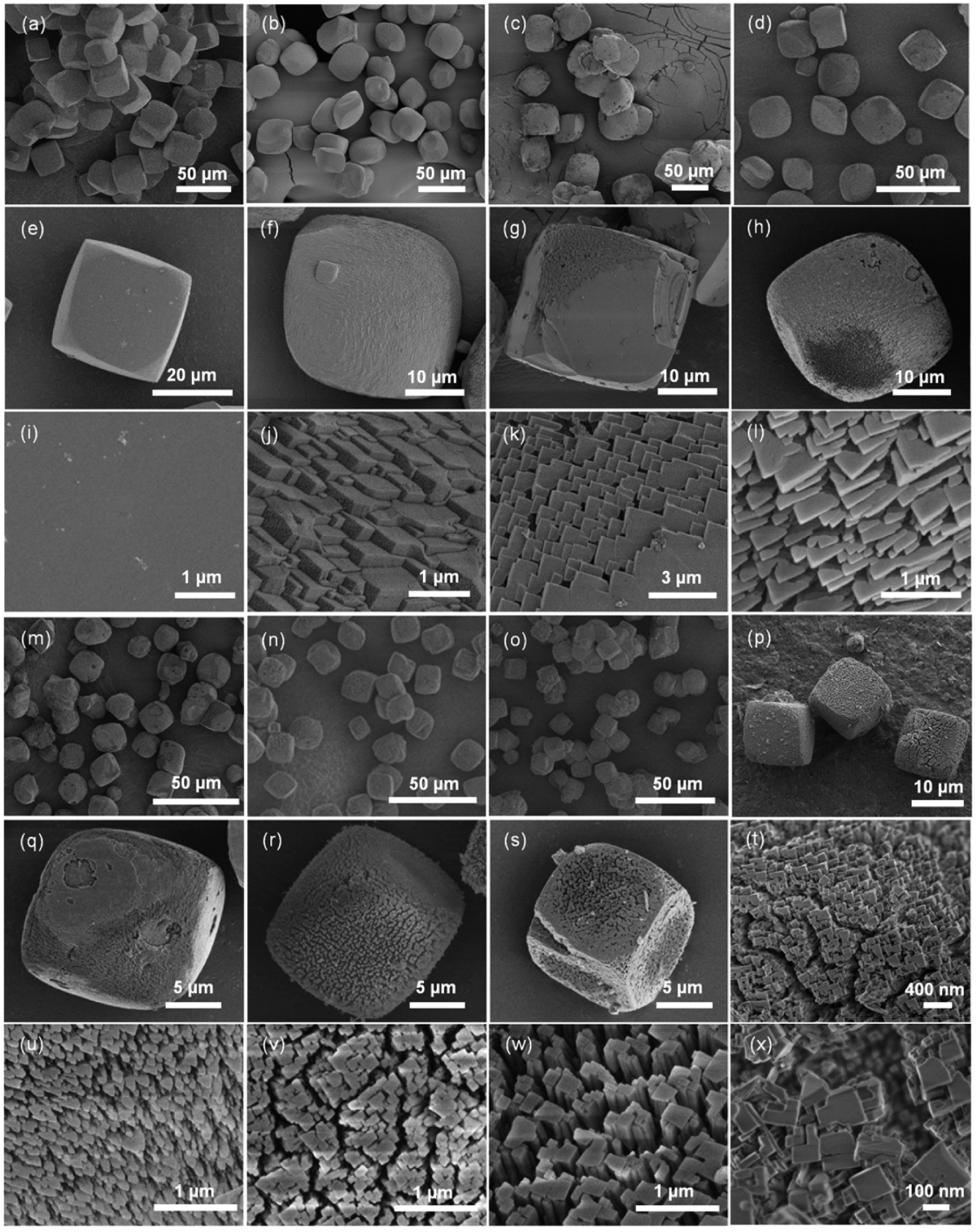

Figure 1. Morphology of SSZ-13 zeolite catalysts. SEM images of (a, e, and i) SSZ-13-R, (b, f, and j) SSZ-13-F, (c, g, and k) SSZ-13-F-M1, and (d, h, and l) SSZ-13-F-M5. (m, q, and u) SSZ-13-F-M10, (n, r, and v) SSZ-13-F-M25, (o, s, and w) SSZ-13-F-M50, and (p, t, and x) LV HRSEM images of SSZ-13-F-M50.

Nuclear magnetic resonance (NMR) spectra were recorded on an 11.7 T Bruker DMX500 NMR spectrometer operating at 500 MHz for ^{1}H, 470 MHz for ^{19}F, 99 MHz for ^{29}Si, and 132 MHz for ^{27}Al measurements. ^{27}Al MAS NMR was performed using a Bruker 2.5 mm MAS probe head spinning at 20 kHz. The MAS NMR measurements were carried out using a 4 mm MAS probe head with sample rotation rates of 10 kHz for ^{1}H and ^{19}F and 5−8 kHz for ^{29}Si NMR measurements. ^{1}H NMR spectra were recorded with a Hahn-echo pulse sequence p_1-τ_1-p_2-τ_2-aq with a 90° pulse p_1 = 5 μs and 180° p_2 = 10 μs. The interscan delay was set to 120 s for quantitative spectra. ^{27}Al 3QMAS NMR spectra were recorded by the use of the three-pulse sequence p_1-t_1-p_2-τ-p_3-t_2 for triple-quantum generation and zero-quantum filtering (strong pulses p_1 = 3.4 μs and p_2 =

DOI: 10.1021/acscatal.5b02480
ACS Catal. 2016, 6, 2163−2177

1.4 μs at ν_1 = 100 kHz; soft pulse p_3 = 11 μs at ν_1 = 8 kHz; filter time τ = 20 μs; interscan delay of 0.2 s). ^{1}H-{^{27}Al} transfer of population in double resonance (TRAPDOR) spectra were measured using a Hahn-echo 90°-τ-180°-τ proton pulse sequence with time interval τ_1 = 795 μs. Two sets of spectra were recorded, with and without irradiation at the ^{27}Al NMR frequency. The same experiment without ^{27}Al irradiation served as a blank experiment for reference purposes. Quantitative ^{29}Si NMR spectra were recorded using a high power proton decoupling direct excitation (DE) pulse sequence with a 54° pulse duration of 3 μs and an interscan delay of 120 s. Higher interscan delay did not show any significant increase in signal intensity. ^{19}F MAS NMR spectra were recorded applying a Hahn-echo pulse sequence and a delay time of 5 s. For ^{1}H MAS NMR measurements, the zeolites were first subjected to a dehydration procedure. A known amount of sample was placed in a glass tube. This tube was connected to a vacuum line, and the sample was dehydrated in this way at a temperature of 450 °C at a pressure lower than 10^{-5} mbar for 6 h. After evacuation, the dehydrated zeolites were placed into the 4 mm MAS NMR zirconia rotor under inert conditions and transferred to the NMR probe head. ^{1}H and ^{29}Si NMR shifts were calibrated using tetramethylsilane (TMS). A saturated aqueous $Al(NO_3)_3$ solution was used for ^{27}Al NMR shift calibration. The intensities of the different components in the ^{1}H and ^{29}Si MAS NMR spectra were obtained by deconvolution using DMfit2011.[29]

FT-IR spectra of CO, pyridine, and propylene adsorbed on the zeolite samples were recorded in the range of 4000−400 cm^{-1} on a Bruker Vertex 70v instrument. The spectra were acquired at 2 cm^{-1} resolution and averaged over 60 scans. The samples were prepared as thin self-supporting wafers (~10 mg cm^{-2}) and placed inside a controlled environment IR transmission cell capable of heating and cooling, gas dosing, and evacuation. Prior to CO adsorption, the catalyst wafer was heated to 550 °C at a rate of 2 °C min^{-1} in oxygen atmosphere. Subsequently, the cell was outgassed at the final temperature until the residual pressure was below 5 × 10^{-5} mbar. For CO (Praxair, 99.999%) adsorption, the sample was cooled to −196 °C, and CO was introduced into the sample cell via a sample loop (5 μL) connected to a Valco six-port valve. For pyridine adsorption, pyridine was introduced to the cell from an ampule kept at room temperature. The exposure time was 20 min followed by desorption for 1 h under evacuation at temperatures of 150, 300, and 500 °C. Spectra were recorded after cooling the sample to 150 °C. FT-IR spectra of propylene were performed at 30 °C; propylene was added by using a 10 μL sample loop. Spectra were normalized to the weight of the catalyst wafer.

In situ visible light microspectroscopy measurements were performed on an Olympus BX41 upright microscope using a 50 × 0.5 NA long working distance microscope objective lens. A 75 W tungsten lamp was used for illumination. The microscope was equipped with a 50/50 double viewport tube, which accommodates a CCD video camera (ColorView IIIu, Soft Imaging Systems GmbH) and an optical fiber mount. A 200 μm core fiber connects the microscope to a CCD UV−vis spectrometer (AvaSpec-2048TEC, Avantes BV). The measurements were conducted in a Linkam FT-IR 600 in situ cell. Before the MTO reaction, the catalysts were heated at a rate of 10 °C min^{-1} to 550 °C in 50 mL min^{-1} of N_2 flow and kept at this temperature for 1 h. Then, the temperature was lowered to 350 °C, and methanol was introduced to the cell by leading a flow of 10 mL min^{-1} of N_2 through liquid methanol kept at room temperature.

A Nikon Eclipse LV150 upright microscope with a 50 × 0.55 NA dry objective was used for fluorescence microscopy studies. Fluorescence microphotographs were collected using 510−700 nm excitation light from a mercury source. Confocal images of spent crystals after the MTO reaction were acquired with a Nikon D-Eclipse C1 head connected to 488, 561, and 635 nm excitation lasers. The emission was detected in the ranges 510−550, 570−620, and 662−737 nm, respectively. For the confocal images of SSZ-13 samples after the exposure to propylene, the excitation wavelength of the laser was 561 nm and detection was in the 570−620 nm range. Thiophene and 4-fluorostyrene oligomerization reactions were performed on the heating element of a Linkam in situ cell. The samples were heated at 120 °C for 5 min. Subsequently, 15 μL of thiophene or 4-fluorostyrene was added, and heating was stopped after 10 s. The fluorescent images were taken by exciting the oligomers with a 561 nm laser and collecting the fluorescent light in the range of 570−620 nm.

Catalytic Activity Measurements. The zeolites were pressed into pellets, which were then crushed and sieved to obtain particles in the range of 250−500 μm. Catalytic activity measurements were carried out in a quartz tubular fixed-bed reactor with 50 mg of catalyst loading. The inner diameter of the quartz tube reactor is 4 mm. Prior to the reaction, the catalyst was activated at 550 °C in synthetic air (30 mL min^{-1}) for 2 h. The MTO reaction was performed at 350 °C. Methanol (Merck, 99%) was introduced to the reactor by leading a flow of 30 mL min^{-1} of He through a saturator kept at −17.2 °C. The resulting WHSV is 0.8 g g^{-1} h^{-1}. The product effluent was analyzed by online gas chromatography (Compact GC Interscience equipped with TCD and FID detectors with RT-Q-Bond and Al_2O_3/KCl columns, respectively). The reaction was followed for 24 h. Thereafter, the catalyst was cooled in He to room temperature and reclaimed as spent catalyst. Methanol conversion is based on the inlet and outlet concentrations of methanol as determined by GC analysis of the reactor feed before and after the reaction and the reactor effluent during the reaction. Dimethyl ether was considered as a reactant in the calculation of the conversion and selectivity.

RESULTS AND DISCUSSION

Structural and Textural Characterization. According to XRD (Figure S1), all materials are phase-pure zeolites with the CHA structure. Figure 1 displays representative SEM images of these zeolites. All samples comprise micron-sized cubic particles with rounded edges. Close inspection of these images highlights that the surface of SSZ-13-R is much smoother than that of SSZ-13-F. The large zeolite particles of SSZ-13-F consist of smaller cubic-shaped crystals (as seen in Figure 1j). The SEM images of the SSZ-13-F-M*x* zeolites show a very open structure consisting of mesoporous voids between crystalline domains. This morphology is similar to the morphology of mesoporous SSZ-13 zeolites prepared with the same mesoporogen but without NaF in the synthesis gel.[19] The SSZ-13-F-M*x* zeolite crystals became slightly smaller when more C_{22-4-4}·Br_2 was used during synthesis. This can be explained by interruption of zeolite crystal growth by the diquaternary ammonium mesoporogen.[19] In high-resolution low-voltage SEM images (Figure 1p, t, and x), SSZ-13-F-M50 zeolite particles were seen to be made up of intergrown primary small crystals that do not contain mesopores themselves.

DOI: 10.1021/acscatal.5b02480
ACS Catal. 2016, 6, 2163−2177

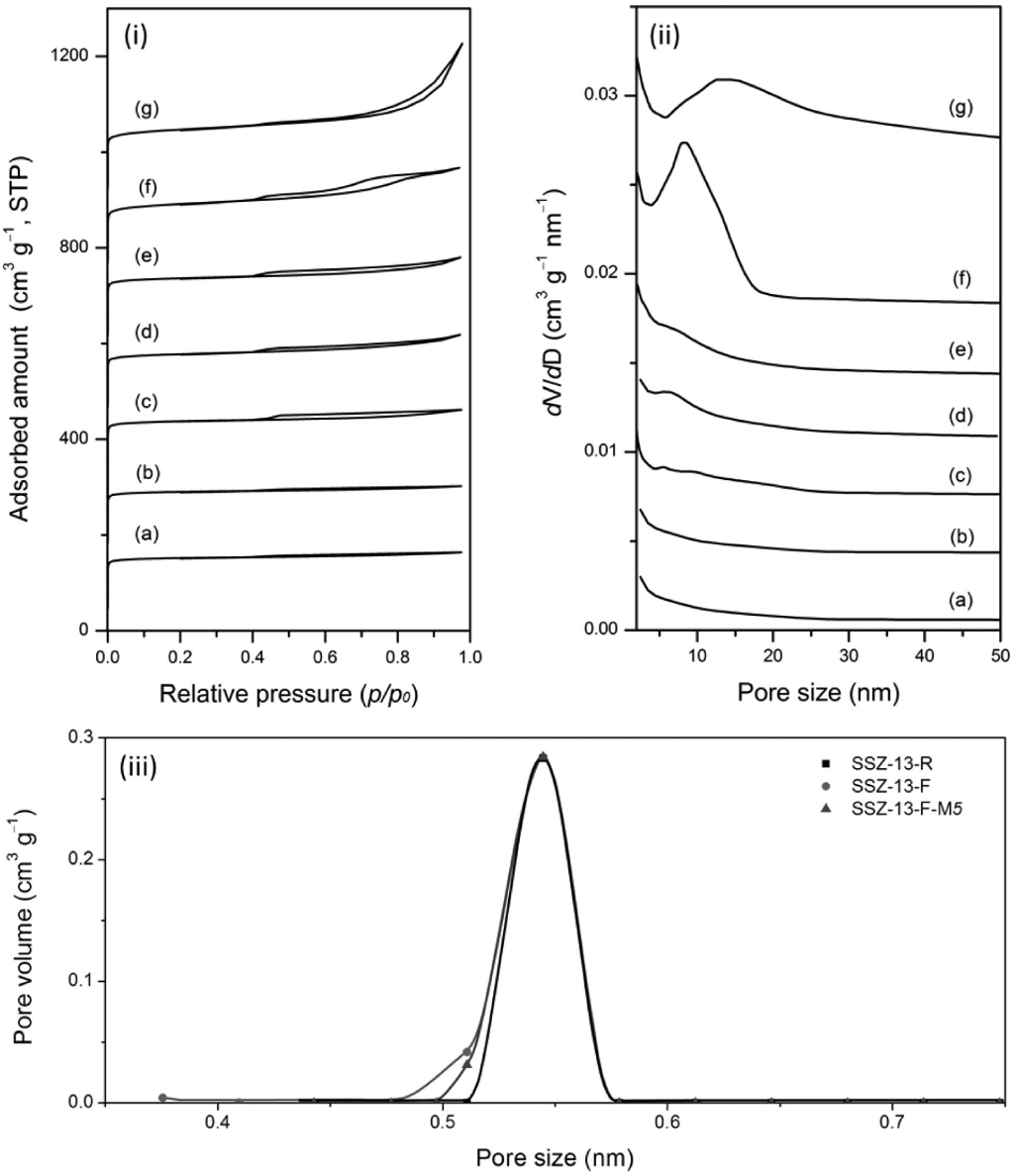

Figure 2. (i) Ar physisorption isotherms and (ii) mesopore size distributions of (a) SSZ-13-R, (b) SSZ-13-F, (c) SSZ-13-F-M1, (d) SSZ-13-F-M5, (e) SSZ-13-F-M10, (f) SSZ-13-F-M25, and (g) SSZ-13-F-M50. (iii) The micropore size distributions analyzed by the NLDFT method point to additional microporosity with a size of ∼0.5 nm. The isotherms were vertically offset by equal intervals of 150 $cm^3\ g^{-1}$. The mesopore size distributions were calculated by the BJH algorithm using the adsorption branch vertically offset by equal intervals of 0.004 $cm^3\ g^{-1}\ nm^{-1}$.

Table 1. Textural Properties of Calcined SSZ-13 Zeolites

zeolite	S_L [a] ($m^2\ g^{-1}$)	V_{tot} [b] ($cm^3\ g^{-1}$)	V_{meso} [c] ($cm^3\ g^{-1}$)	V_{micro} [d] ($cm^3\ g^{-1}$)	S_{micro} [d] ($m^2\ g^{-1}$)	S_{ext} [d] ($m^2\ g^{-1}$)
SSZ-13-R	677	0.24	0.02	0.20	643	34
SSZ-13-F	763	0.28	0.03	0.23	705	58
SSZ-13-F-M1	707	0.27	0.04	0.21	636	71
SSZ-13-F-M5	778	0.29	0.05	0.22	672	106
SSZ-13-F-M10	745	0.30	0.07	0.21	632	113
SSZ-13-F-M25	787	0.36	0.12	0.21	644	143
SSZ-13-F-M50	754	0.48	0.25	0.19	629	124

[a] S_L is the Langmuir surface area obtained in the relative pressure range (p/p_0) of 0.05−0.20. [b] V_{tot} is the total pore volume at p/p_0= 0.97. [c] V_{meso} is the mesopore volume calculated by the BJH method. [d] V_{micro} (micropore volume), S_{micro} (micropore surface area), and S_{ext} (external surface area) are calculated by the *t*-plot method.

Figure 2 shows the Ar physisorption isotherms and the corresponding pore size distributions of the calcined SSZ-13 zeolite samples. The isotherms of SSZ-13-R and SSZ-13-F are typical for microporous materials. The textural properties listed in Table 1 show that these two zeolites contain hardly any mesopores. The micropore volume and Langmuir surface area

DOI: 10.1021/acscatal.5b02480
ACS Catal. 2016, 6, 2163−2177

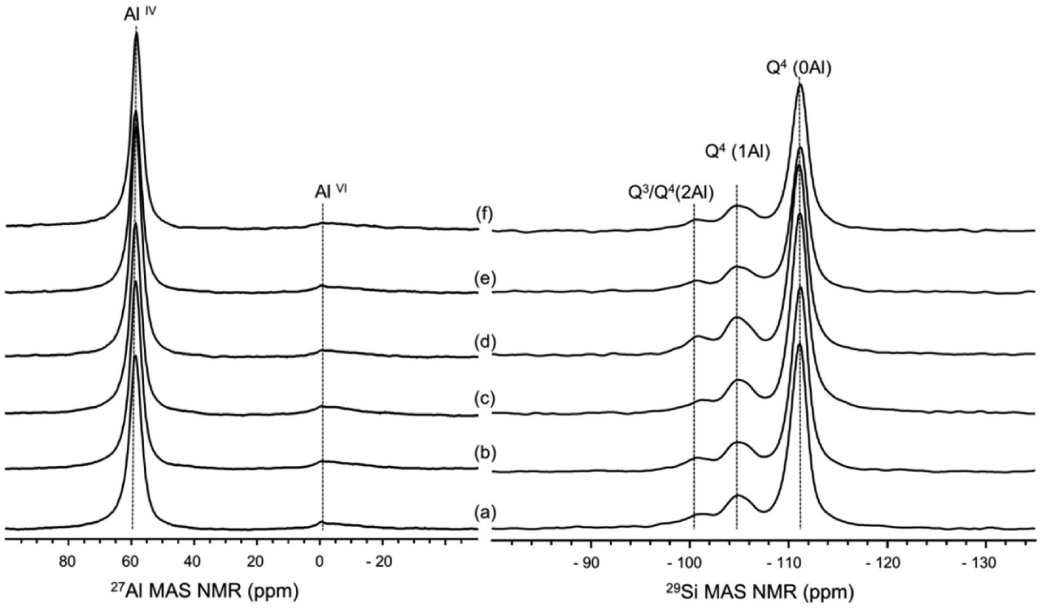

Figure 3. (left) ^{27}Al and (right) ^{29}Si MAS NMR spectra of (a) SSZ-13-R, (b) SSZ-13-F, (c) SSZ-13-F-M5, (d) SSZ-13-F-M10, (e) SSZ-13-F-M25, and (f) SSZ-13-F-M50. The spectra are normalized by the weight of the samples.

for SSZ-13-F are larger as compared with those of SSZ-13-R. The micropore size distribution of SSZ-13-R, SSZ-13-F, and SSZ-13-F-M5 zeolites were analyzed by the NLDFT method. The micropore size distribution of SSZ-13-R centers around 0.54 nm,[30,31] which is the effective diameter considering that the pore system of CHA is a combination of cages and pore apertures with sizes of 0.92 and 0.38 nm, respectively. The NLDFT micropore size distributions of SSZ-13-F and SSZ-13-F-M5 contain a shoulder that is due to additional micropores that are larger than the size of the pore apertures of CHA zeolite (0.38 nm). The additional microporosity of SSZ-13-F-M5 is only slightly lower than that of SSZ-13-F. We hypothesize that, in a gel system containing hydroxide and fluoride anions, OH^- will compete for the charge-balancing role with fluoride anions.[32] The formation of less-soluble fluorinated inorganic precursor units would lead to limited Ostwald ripening and high supersaturation of the synthesis gel. Accordingly, the zeolite will predominantly grow via adhesive growth.[33] We speculate that the additional micropores are located at the grain boundaries of the primary nanocrystals.[28] All SSZ-13-F-M*x* zeolites display type IV adsorption isotherms, characteristic for the combined presence of micropores and disordered mesopores. The textural properties show that all mesoporous SSZ-13 zeolites have larger surface areas than those of the microporous reference zeolite. The SSZ-13-F-M25 sample has the highest Langmuir surface area (787 $m^2\ g^{-1}$). The micropore volumes of SSZ-13-F and SSZ-13-F-M*x* are close to that of SSZ-13-R, which confirms the high crystallinity of these zeolite samples. The observation that the zeolite prepared with the highest amount of mesoporogen in the synthesis gel has the largest mesopore is in keeping with the role of $C_{22-4-4}{\cdot}Br_2$ in mesopore generation.

^{27}Al MAS NMR spectra of the synthesized SSZ-13 zeolites are shown in Figure 3. The main feature at ∼59 ppm in all spectra is due to a symmetric tetrahedrally coordinated Al species (Al^{IV}) associated with Al atoms in the CHA zeolite framework.[34] The asymmetrically broadened peaks located at ∼0 ppm represent extraframework Al in octahedral coordination (Al^{VI}). Deconvolution of these spectra (Table 2) shows that ∼90% of the Al atoms are located in the zeolite framework. The Si/Al ratios of all the samples measured by ICP-OES elemental analysis were also very similar. ^{27}Al 3QMAS NMR spectra (Figure S2) reveal that there is no difference in the Al speciation between SSZ-13-R and SSZ-13-F.

Table 2. Si/Al Ratio Determined by ICP-OES Elemental Analysis and ^{29}Si MAS NMR[a]

zeolite	Si/Al (ICP)	Si/Al[b] (^{29}Si NMR)	Al^{IV} (%)	Al^{VI} (%)
SSZ-13-R	21	22	89	11
SSZ-13-F	22	25	88	12
SSZ-13-F-M5	22	26	86	14
SSZ-13-F-M10	22	22	88	12
SSZ-13-F-M25	23	22	93	7
SSZ-13-F-M50	23	23	92	8

[a]The relative amount of the Al species in zeolites was determined by ^{27}Al MAS NMR. [b]Deconvoluted according to the strategy outlined by Eilertsen et al.[36]

The coordination of the Si atoms in the zeolites was determined by DE ^{29}Si MAS NMR spectroscopy (Figure 3). ^{29}Si MAS NMR allows determining the framework Si/Al ratio $(Si/Al)_F$ from the relative intensities of tetrahedral Si (Q^4) with different numbers of Al atoms in the second coordination sphere $Q^4(n\mathrm{Al})$ with n = 0, 1, 2, 3, or 4 by use of $(Si/Al)_F = 4(\Sigma I_n)/(\Sigma n I_n)$, where I is the peak area and n is the number of coordinated Al atoms.[35] All spectra contain three distinct signals at −101, − 105, and −111 ppm, which can be assigned to $Q^4(2Al)$, $Q^4(1Al)$, and $Q^4(0Al)$, respectively. As the signal at approximately −101 ppm consists of overlapping peaks from $Q^4(2Al)$ and Si atoms with terminal hydroxyl groups at the defect sites $Si(SiO)_3OH$ (Q^3), the spectra were deconvoluted according to the strategy outlined by Eilertsen et al.[36] The calculated framework Si/Al ratios of the different materials are comparable to the Si/Al ratios determined by ICP-OES.

Acidity Characterization. The nature of the OH groups of the SSZ-13 zeolites was investigated by means of ^{1}H MAS NMR and IR spectroscopy of adsorbed CO. Quantitative ^{1}H MAS NMR spectra of the dehydrated samples are shown in

DOI: 10.1021/acscatal.5b02480
ACS Catal. 2016, 6, 2163−2177

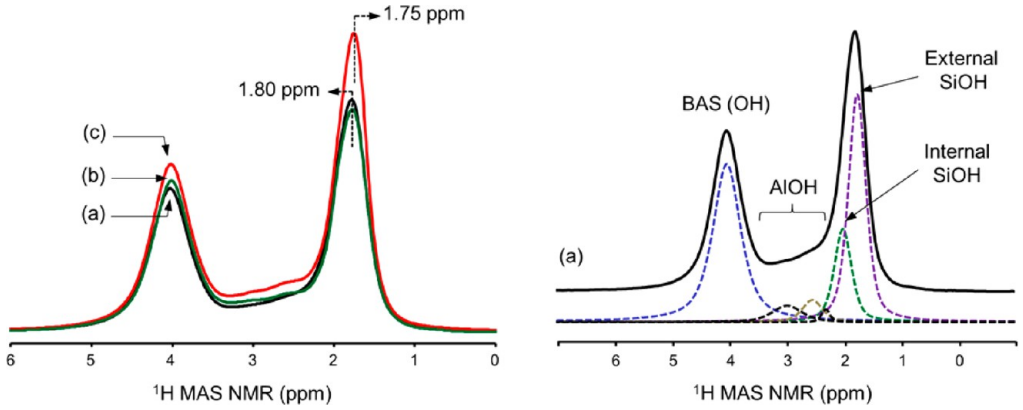

Figure 4. ^{1}H MAS NMR spectra of (a) SSZ-13-R, (b) SSZ-13-F, and (c) SSZ-13-F-M25. The right figure shows the deconvolution of the spectra for SSZ-13-R. The spectra were normalized to the catalyst weight.

Figure 4. The assignment and results of the deconvolution of these spectra are given in Table 3. Close inspection of ^{1}H T_2-filtered spectra (Figure S3) shows that the silanol signal consists of two signals at 2.0 and 1.8 ppm. The signal at 1.8 ppm is due to isolated external silanol groups at lattice defect sites. The downfield shift of the resonance at 2.0 ppm refers to the interaction of silanol groups with neighboring oxygen atoms, indicating that they are located in the zeolite micropores.[37−40] These two distinct groups of silanols were also observed by FTIR characterization (vide infra). Notably, the silanol band in SSZ-13-F-M25 shifted upfield compared with the two microporous zeolites due to the significantly higher content of silanol groups at the surface, which experience less hydrogen bonding than the internal silanol groups. The band at ∼4 ppm belongs to the bridging OH groups in Si(OH)Al moieties (Brønsted acid sites, BAS).[41,42] Signals in the region 2.5−3.0 ppm correspond to OH groups of AlOH moieties at extraframework positions.[42,43] These assignments are supported by data from ^{1}H-{^{27}Al} TRAPDOR NMR experiments (Figure S4). This technique helps to identify the protons located in the vicinity of Al atoms.[44] Results of deconvolution of these spectra, which are summarized in Table 3, show that SSZ-13-R and SSZ-13-F zeolites have similar densities of external silanols. SSZ-13-F contains fewer internal silanol defects than SSZ-13-R, which can be ascribed to charge compensation by fluoride anions during the zeolite growth process. The number of internal silanol defects for SSZ-13-F-M25 is intermediate to values for SSZ-13-R and SSZ-13-F. All samples contain strong BAS in nearly the same amount. Finally, ^{19}F MAS NMR (Figure S5) revealed that there is no fluoride retained in the samples after the template was removed by calcination.

Table 3. Integrals of Deconvoluted ^{1}H MAS NMR Spectra of Dehydrated SSZ-13-R, SSZ-13-F, and SSZ-13-F-M25 and External BAS Density As Determined by IR of Adsorbed Pyridine

zeolite	BAS_{total} [a] (mmol g^{-1})	$BAS_{external}$ [b] (mmol g^{-1})	$SiOH_{external}$ [a] (mmol g^{-1})	$SiOH_{internal}$ [a] (mmol g^{-1})
SSZ-13-R	0.65	0.00	0.55	0.22
SSZ-13-F	0.67	n.d.[c]	0.55	0.17
SSZ-13-F-M25	0.80	0.04	0.77	0.19

[a]Determined by ^{1}H MAS NMR. [b]Determined by IR of adsorbed pyridine. [c]Not determined (n.d.).

The acidity situation of the zeolites was investigated in more detail by FTIR spectra of adsorbed CO and pyridine. CO IR spectra are given in Figure 5 and show strong bands in the OH stretching region between 3900 and 3100 cm^{-1}. Bands at 3735 and 3707 cm^{-1} are assigned to isolated external and internal silanols, respectively. The band at 3500 cm^{-1} relates to silanol nests.[12] The band at ∼3610 cm^{-1} is due to acidic bridging OH groups in H-SSZ-13 zeolite.[45,46] Upon CO adsorption, the band of these BAS shifts to 3308 cm^{-1} for all samples, indicating similar acid strength of the BAS. This result is evidence that the use of fluoride and the $C_{22-4-4}{\cdot}Br_2$ mesoporogen did not influence the strength of the acid sites.

As the size of pyridine is too large to enter the pores of CHA zeolite, BAS probed by pyridine in this way are located outside the micropore space of the zeolites (Figure 6, Table 3). The bands in the spectra at ∼1455, 1490, and 1545 cm^{-1} arise from pyridine interacting with Lewis acid sites (LAS), LAS and BAS sites, and BAS, respectively.[47] The concentration of BAS at the external crystal surface of SSZ-13-R is negligible. On the contrary, such sites can be clearly observed for SSZ-13-F-M25 because of its higher surface area. It is estimated that approximately 5% of all of the BAS are located at the external crystal surface in SSZ-13-F-M25.

The investigations described above show the changes of physicochemical properties in zeolites synthesized with or without NaF as well as how the mesoporogen affects them. All samples have similar Si/Al ratios, and the concentration and strength of the BAS are also very similar in all zeolites. The use of $C_{22-4-4}{\cdot}Br_2$ in the synthesis gel results in mesoporosity in the zeolite crystals and also slightly affects the crystal size. The other significant difference appears to be the lower internal silanol content of the samples prepared in the presence of NaF. This is due to the role of fluoride as charge-compensating anions, which lowers the number of defects during the synthesis of high-silica zeolites.[23,48] The presence of a small amount of F^- ions in the alkaline synthesis gel of SSZ-13 influences the growth process of SSZ-13 zeolite,[28] and as a result, the obtained SSZ-13-F zeolite contains an additional micropore system with pores that are ∼0.5 nm in size. Although zeolites including H-SSZ-13 can also be synthesized in fluoride media at near-neutral pH,[49] this route cannot be used in combination with the $C_{22-4-4}{\cdot}Br_2$ mesoporogen, as $C_{22-4-4}{\cdot}Br_2$ cannot be dispersed

DOI: 10.1021/acscatal.5b02480
ACS Catal. 2016, 6, 2163−2177

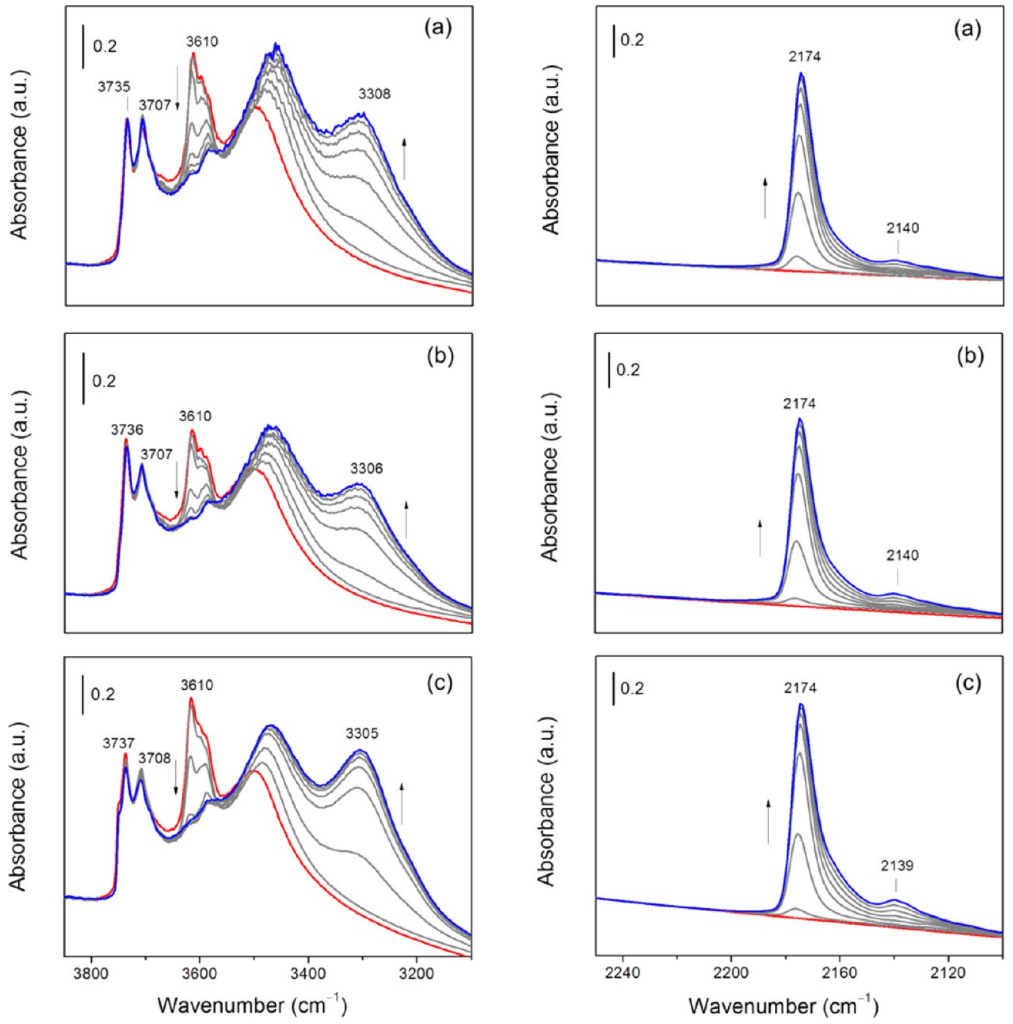

Figure 5. (left) Hydroxyl and (right) CO stretch regions of FTIR spectra of (a) SSZ-13-R, (b) SSZ-13-F, and (c) SSZ-13-F-M25 as a function of the CO coverage. The spectra were normalized by the weight of the catalysts.

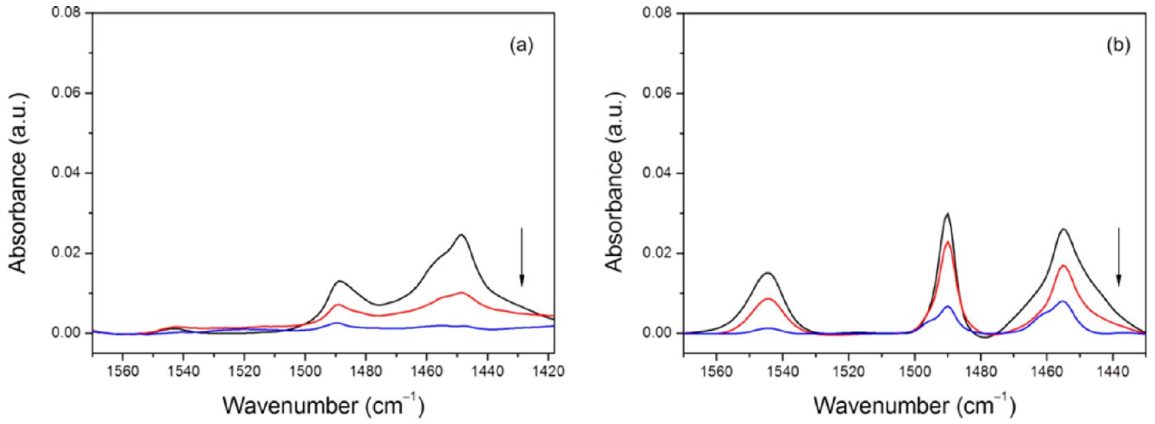

Figure 6. Infrared spectra of pyridine adsorbed on the proton forms of (a) SSZ-13-R and (b) SSZ-13-F-M25 after evacuation at 150, 300, and 500 °C (arrow indicates increasing evacuation temperature); IR spectra were recorded at 150 °C.

well enough in the very viscous (low H_2O/SiO_2 = 3) synthesis gels used in fluoride-mediated zeolite synthesis.

To confirm that the SSZ-13-F zeolite crystals contain additional micropores, we made use of a staining technique involving fluorescent oligomers of thiophene and 4-fluorostyrene that can be detected by confocal fluorescence spectroscopy. The oligomerization of thiophene and 4-fluorostyrene is catalyzed by BAS.[50,51] The confocal fluorescence microscopy images taken in the middle plane of zeolite SSZ-13 crystals, which are shown in Figure 7, show that no fluorescent species formed inside the crystal of the SSZ-13-R sample. This is because the kinetic diameters of thiophene or 4-fluorostyrene are larger than the pore apertures of the CHA framework (0.38 nm). On the contrary, the stained crystal of SSZ-13-F showed

DOI: 10.1021/acscatal.5b02480
ACS Catal. 2016, 6, 2163−2177

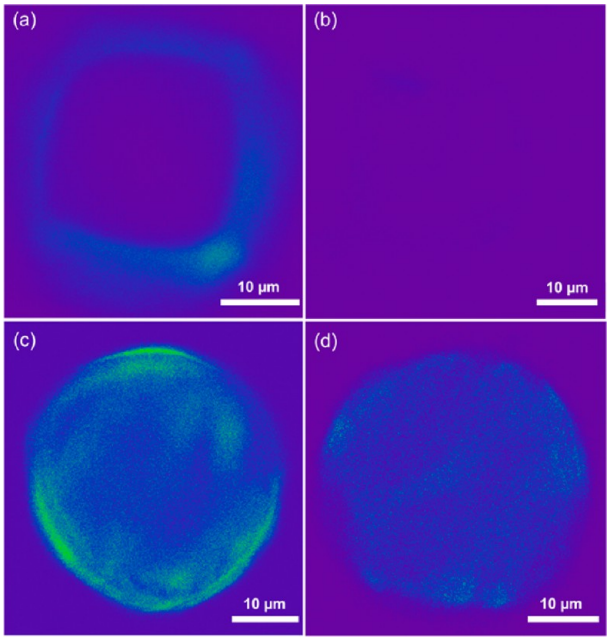

Figure 7. Confocal fluorescence microphotographs of (a, b) SSZ-13-R and (c, d) SSZ-13-F crystals collected after the (a, c) thiophene and (b, d) 4-fluorostyrene oligomerization reactions. The images were taken in the middle plane of single crystals.

fluorescence throughout the crystal (Figure 7c, d). These results strongly indicate that SSZ-13-F contains micropores throughout the zeolite crystal that are larger than the size of the CHA pore apertures.

Effect of Hierarchical Structure on Diffusion. The influence of the additional intracrystalline micropores and mesopores on the diffusion was investigated by comparing the uptake of different organic molecules at 30 °C in the dehydrated zeolites by thermogravimetric analysis. We first established that the total uptake of methanol by SSZ-13-R and SSZ-13-F were very similar (Figure 8a). Their uptake is ∼120 mg g^{-1}. This corresponds to approximately 5 methanol molecules per BAS, close to the value reported for methanol uptake in SAPO-34.[52] It implies that the adsorption is dominated by weakly adsorbed methanol molecules in addition to a small amount of protonated methanol molecules. As the uptake rates were seen to be similar for both zeolites, we conclude that the difference in porosity did not affect the diffusion rate of methanol. The uptake rate of methanol by SSZ-13-F-M25 is much higher, and the amount of methanol taken up is also higher as compared with those of SSZ-13-R and SSZ-13-F. This indicates that the mesopores and shortened diffusion length in the mesoporous SSZ-13 samples facilitate the mass transport of methanol and increase adsorption capacity. The additional pore volume due to the mesopores explains the higher total uptake of methanol. Panels b and c in

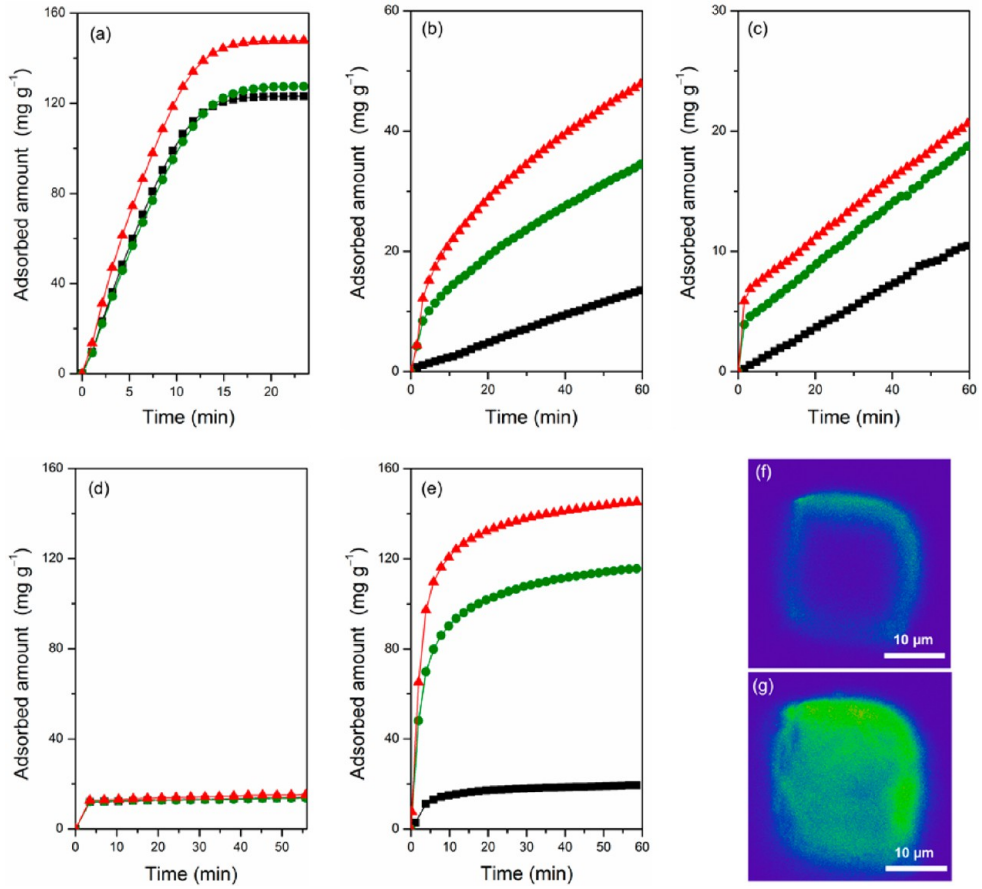

Figure 8. (a) Methanol, (b) *n*-butanol, (c) *i*-butanol, (d) ethylene, and (e) propylene uptake experiments performed at 30 °C on zeolite samples (black squares) SSZ-13-R, (green circles) SSZ-13-F, and (red triangles) SSZ-13-F-M25. The samples were dehydrated before the adsorption. Confocal fluorescence images of (f) SSZ-13-R and (g) SSZ-13-F crystals collected after the propylene adsorption. The images were taken in the middle plane of single crystals and are shown in false colors.

DOI: 10.1021/acscatal.5b02480
ACS Catal. 2016, 6, 2163−2177

Figure 8 also show that the uptake of larger molecules, such as *n*-butanol and *i*-butanol, strongly differs between SSZ-13-R, SSZ-13-F, and SSZ-13-F-M25. The slow uptake of butanols in the SSZ-13-R sample is consistent with the slow reported uptake of linear alcohols in SAPO-34.[53] The total uptake increases in the order SSZ-13-R < SSZ-13-F < SSZ-13-F-M25 for both adsorbates. The uptake data also show that butanols are initially adsorbed faster in SSZ-13-F and SSZ-13-F-M25 than in SSZ-13-R. The initial uptake of the former two samples is very similar, from which we derive that the rapid uptake of butanols is due to the additional micropores. These micropores appear to affect the initial uptake rate more than that of the mesopores in SSZ-13-F-M25. We explain this by the fact that the additional micropores decrease the crystalline CHA zeolite domain size more than the mesopores. Another factor may be the higher heat of adsorption of butanols in these micropores than in the mesopores.

The uptake of light olefins was also investigated for these zeolites. Panels d and e in Figure 8 show the uptake curves for ethylene and propylene, respectively. The uptake of propylene increases in the order SSZ-13-R < SSZ-13-F < SSZ-13-F-M25. After 60 min of exposure to propylene, the adsorption capacities of SSZ-13-R, SSZ-13-F, and SSZ-13-F-M25 are 0.46 (0.71), 2.75 (4.10), and 3.46 (4.33) mmol g^{-1} (number of propylene molecules per BAS in brackets), respectively. Propylene is very reactive and can be protonated already at room temperature by the BAS of the zeolites.[54] The resulting adsorbed propyl carbenium ion can then further react with propylene to oligomers. This is proven by IR spectra of these samples after exposure to propylene for prolonged time at room temperature (Figure S6). Bands at 2962, 2937, 2871, 1466, and 1380 cm^{-1} in the resulting IR spectra can be assigned to propylene oligomers.[54] These spectra also show that SSZ-13-F contains more of these oligomers than SSZ-13-R. Confocal fluorescence images of these two zeolites after exposure to propylene (as shown in Figure 8f and g) reveal that pore blocking by oligomers in the outer regions of the SSZ-13-R crystal explains the low propylene uptake compared with the other two zeolites. Figure 8d shows that only a small amount of ethylene is taken up by the zeolites. Because of the lower reactivity of ethylene, it is mainly physically adsorbed in the micropores. As oligomerization does not occur, there will also be no pore blocking in this case, and all three samples behave similarly.

Catalytic Performance in the MTO Reaction. The zeolites were then evaluated for their catalytic performance in the MTO reaction at 350 °C. It has been reported that the optimum MTO reaction temperature for SSZ-13 is in the range 350−375 °C, which is lower than the optimum reaction temperature for SAPO-34.[12] The methanol conversion as a function of time on stream is shown in Figure 9. The catalyst lifetime is usually defined as the time to reach a conversion of 50% (t_{50}). Here, we also employ the time at which conversion has decreased to 98% (t_{98}), as this is more relevant for commercial practice. The corresponding data including the product selectivities at 98% methanol conversion are collected in Table 4. During the initial stages of the reaction, all zeolite catalysts converted the methanol feed completely and produced ethylene and propylene with a combined yield above 80%. The methanol conversion of SSZ-13-R decreased drastically with time on stream, and t_{50} (t_{98}) was only 5.1 h (2.1 h). SSZ-13-F already showed a much longer t_{50} (t_{98}) of 10.1 h (5.2 h). The set of SSZ-13-F-M*x* zeolites was able to convert methanol for at least 7 h (t_{98}), and their deactivation rates were much lower compared with the two microporous SSZ-13 zeolites. Consequently, their lifetimes were much longer ($t_{50} \approx 14$ h). Although all of the mesoporous zeolites performed quite similarly, the zeolite with the highest mesopore volume was seen to deactivate slowest. Notably, the catalytic behavior of SSZ-13-R-M5 (t_{50} = 9.9 h, Figure S7), mesoporous SSZ-13 prepared without fluoride in the synthesis gel, was better than that of SSZ-13-R yet worse than that of SSZ-13-F-M5. This provides evidence that the combined use of the mesoporogen $C_{22-4-4}{\cdot}Br_2$ and fluoride in SSZ-13 synthesis is synergistic with respect to catalytic MTO performance.

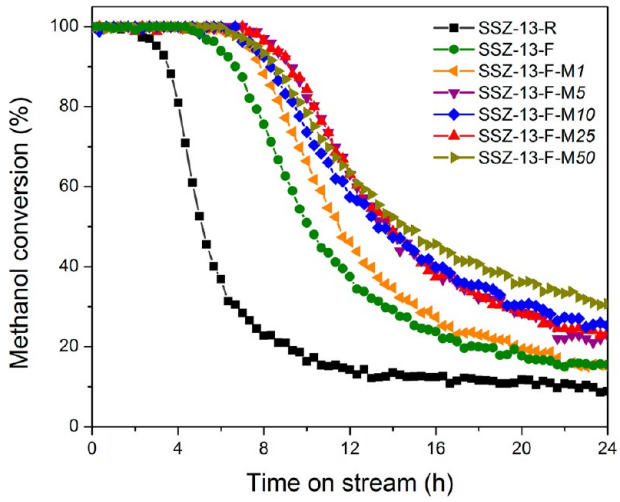

Figure 9. Catalytic performance in the MTO reaction of SSZ-13 zeolites (reaction conditions: T = 350 °C, WHSV = 0.8 g g^{-1} h^{-1}).

The high light olefin selectivity is one of the most important benefits of the use of CHA zeolite in methanol conversion reactions. Among others, the acidity,[55] the reaction conditions,[56] coke,[57] and possible cofeeding approaches[58,59] will affect the product selectivity. The selectivity data for the MTO reaction at 98% methanol conversion show that ethylene and propylene were the main reaction products. We observed that the propylene selectivity slightly decreased with time on stream and, at the same time, the ethylene selectivity increased (Figure S8). We speculate that propylene in part derives from the alkene-based mechanism occurring in larger pores, that is, in the additional micropores in SSZ-13-F and also in the mesopores in the SSZ-13-F-M*x* samples. This explains the higher $C_2^=/C_3^=$ ratio for SSZ-13-R. It might be that the active sites in the larger pores deactivate more rapidly than those involved in the aromatic-based reaction cycle in the CHA supercages. These effects are, however, relatively minor. Earlier, it had been reported that increased diffusion in mesopores increases the C_4-C_6 selectivity.[60] In our case, the C_4-C_6 selectivity was not affected in a systematic manner by the textural properties of the zeolites. This most likely relates to the predominance of the catalytic reaction events in the SSZ-13 micropores, which is consistent with the relatively small fraction of acid sites located in larger pores in the bimodal and trimodal zeolite samples (see Table 3).

We determined the total methanol conversion capacity (TCC) of these zeolites (Figure S9) according to the method proposed by Bjørgen et al.[61] The corresponding data are given in Table 4. It is seen that the TCC increases in the order SSZ-13-R < SSZ-13-F < SSZ-13-F-M1 < SSZ-13-F-M5 ≈ SSZ-13-F-

DOI: 10.1021/acscatal.5b02480
ACS Catal. 2016, 6, 2163−2177

Table 4. Lifetime and Product Selectivity of MTO Reaction at 98% Methanol Conversion over SSZ-13 Zeolites (T = 350 °C; WHSV = 0.8 g g^{-1} h^{-1})

				selectivity (%)					
zeolite	t_{50}[a] (h)	t_{98}[b] (h)	TCC[c] (g g^{-1})	C_1	$C_2^=$	C_2	$C_3^=$	C_3	C_4–C_6[d]
SSZ-13-R	5.1	2.1	6.8	1.1	44.4	0.4	37.7	1.8	14.5
SSZ-13-F	10.1	5.2	12.5	1.1	46.4	0.2	38.1	0.8	13.4
SSZ-13-F-M1	11.5	6.5	14.2	1.1	45.8	0.2	37.3	0.6	15.0
SSZ-13-F-M5	13.7	7.7	16.5	1.2	46.8	0.2	37.8	0.6	13.4
SSZ-13-R-M5	9.9	6.2	11.5	1.0	46.3	0.3	38.1	1.0	13.3
SSZ-13-F-M10	13.9	7.7	16.5	1.2	45.5	0.3	37.0	0.9	15.1
SSZ-13-F-M25	13.8	6.7	16.5	1.2	45.7	0.2	37.9	0.8	14.3
SSZ-13-F-M50	14.3	6.7	20.0	1.2	46.1	0.2	38.2	0.6	13.7

[a]Lifetime is defined as the time to reach 50% of methanol conversion. [b]Lifetime is referred to the time to reach 98% of methanol conversion. [c]Total methanol conversion capacity. [d]Sum of olefin and paraffin selectivity.

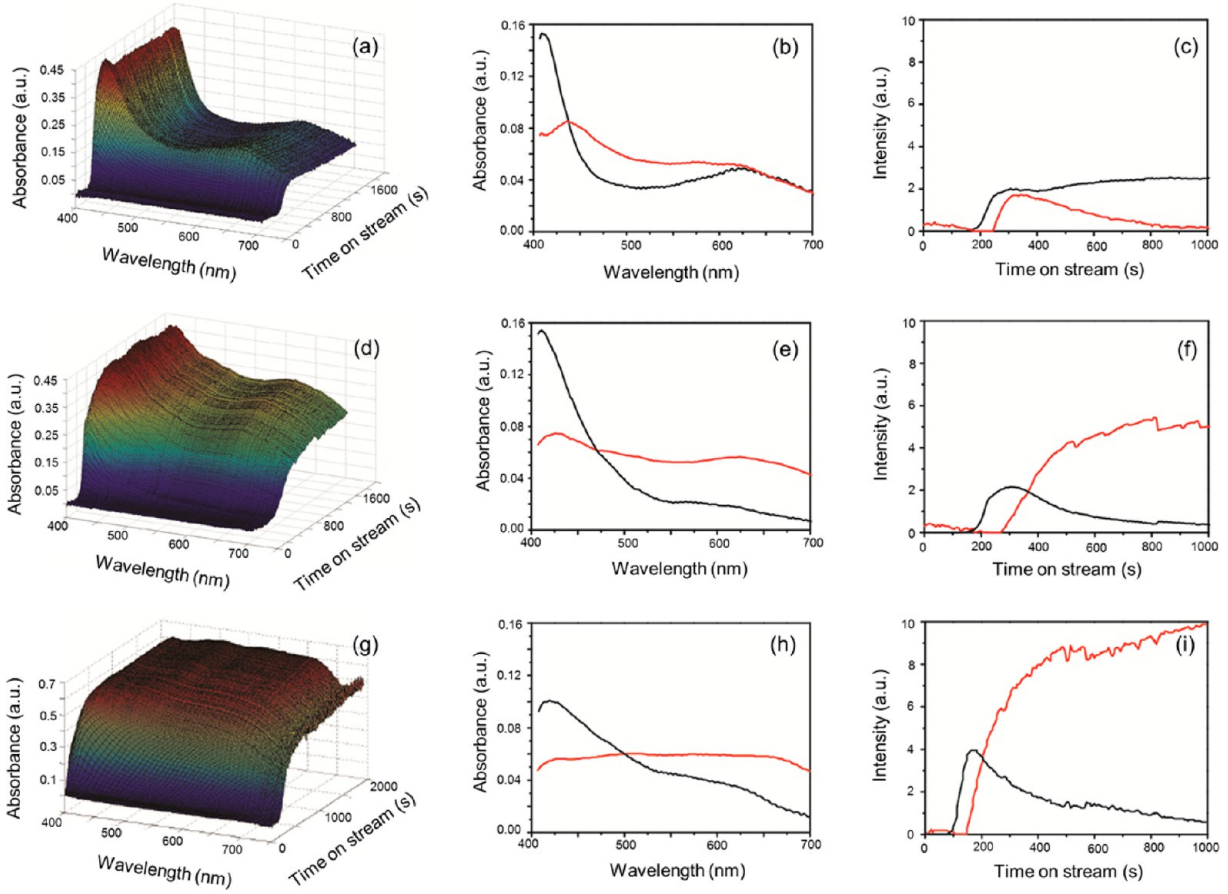

Figure 10. Time-resolved in situ visible spectra of (a, b, and c) SSZ-13-R, (d, e, and f) SSZ-13-F, and (g, h, and i) SSZ-13-F-M25 taken during the MTO reaction at 350 °C. All of the time-resolved spectra can be deconvoluted into two main spectral features (b, e, and h; black line refers to polymethylated benzenes and red line stands for more bulkier polyaromatic species) by non-negative matrix factorization analysis and the evolution of those spectral features with time on stream (c, f, and i). The spectra were taken from a 2 μm spot in the center region of single SSZ-13 crystals.

M10 ≈ SSZ-13-F-M25 < SSZ-13-F-M50. The higher TCC value for SSZ-13-F-M50 is mainly due to the lower rate of deactivation. Nevertheless, the time to the onset of deactivation was very similar for all mesoporous SSZ-13 zeolites.

In industrial practice, MTO catalysts are regenerated by combustion of the carbon deposits in a process layout that is similar to FCC. Therefore, it is important to assess the reusability of new or improved catalysts. For this purpose, spent SSZ-13-F-M25 was regenerated by in situ calcination at 550 °C for 4 h followed by evaluation of its activity under identical conditions as the first activity measurement. This reaction-regeneration cycle was repeated five times. Figure S10 shows that there was no decrease in the catalytic performance in the consecutive cycles.

The textural properties of the spent catalysts after 24 h time on stream were determined by Ar physisorption. The carbon deposit content was determined by thermogravimetric analysis (TGA). The results are given in Table S1. Compared with the fresh samples, the mesopore volumes of the spent catalysts were only slightly lower. On the contrary, the micropore volumes of the spent catalysts decreased very substantially during the MTO reaction. This shows that the carbon

DOI: 10.1021/acscatal.5b02480
ACS Catal. 2016, 6, 2163–2177

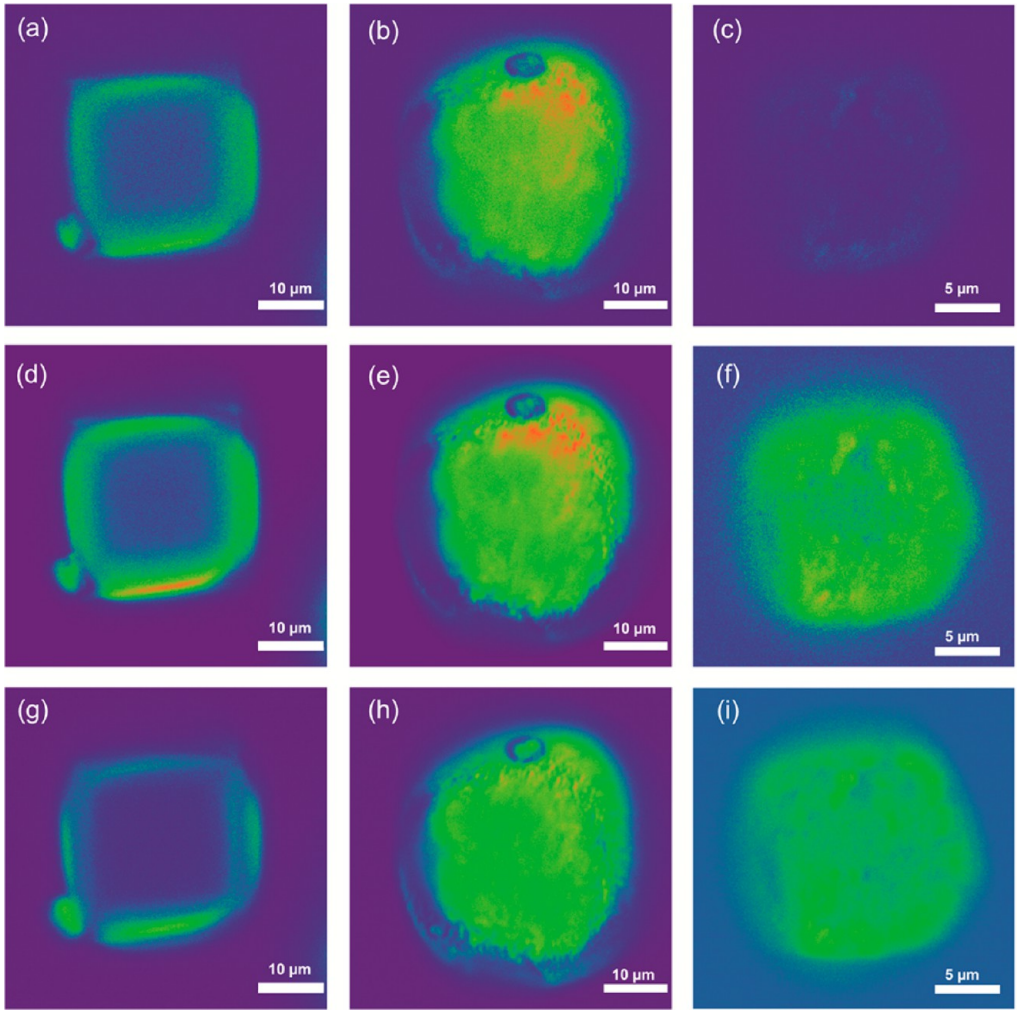

Figure 11. Confocal fluorescence microscopy images of (a, d, and g) SSZ-13-R, (b, e, and h) SSZ-13-F, and (c, f, and i) SSZ-13-F-M25 crystals collected after the MTO reaction. The images were taken in the middle plane of single crystals and are shown in false colors. For the visualization of the coke species, (a, b, and c) 488 nm, (d, e, and f) 561 nm, and (g, h, and i) 635 nm lasers were used with a detection range of 510−550, 570−620, and 662−737 nm, respectively.

deposition mainly takes place in the micropores, consistent with the mechanistic proposal of occluded polymethylated benzenes as reaction centers. There is no clear trend between the remaining micropore volume and the initial mesopore volume. From this, we conclude that either all micropores were filled with carbon deposits or that the pore entrances were blocked. In line with this, we observe that in all cases the Langmuir surface area was much lower after the reaction. Comparing the various samples, SSZ-13-F and SSZ-13-F-M*x* contain more carbon deposits than SSZ-13-R. Less carbon is deposited on the mesoporous SSZ-13 zeolites with increasing mesopore volume. This is due to the fact that the mesoporous zeolites are not fully deactivated after 24 h time on stream, and the catalysts are still able to convert the reactant methanol. Therefore, not all of the zeolite micropores are filled with larger coke deposits.

The present data show that the NaF modification of the alkaline SSZ-13 synthesis can be effectively combined with C_{22-4-4}·Br_2 to generate substantial intracrystalline mesoporous voids in the zeolite crystals. In this way, we obtain trimodal porosity in these crystals. All of the zeolite samples display similar acidity. SSZ-13 synthesized in the presence of NaF and C_{22-4-4}·Br_2 shows strongly improved catalytic performance in the MTO reaction. In our earlier work, we found that the maximum lifetime of ∼8 h in the MTO reaction under the same reaction conditions was obtained for a particular C_{22-4-4}·Br_2/TMAdaOH ratio.[41] The present data show that the optimum performance is already obtained when a very small amount of C_{22-4-4}·Br_2 is added to the fluoride-containing synthesis gel. The combination of NaF in the synthesis gel and a small amount of C_{22-4-4}·Br_2 is therefore effective in obtaining optimal SSZ-13 zeolite catalysts for the MTO reaction.

Coke Formation and Distribution. To better understand the nature of the carbon deposits and their spatial distribution in the zeolite crystals, we investigated SSZ-13-R, SSZ-13-F, and SSZ-13-F-M25 by time-resolved in situ visible light microspectroscopy. The resulting spent samples were also further investigated by confocal fluorescence microscopy. For the purpose of the Vis spectroscopy measurements, a few zeolite crystals were placed in the in situ cell and exposed to a nitrogen flow saturated with methanol at a total flow rate of 10 mL min^{-1}. The reaction temperature was 350 °C. In this configuration, we cannot accurately determine the weight hourly space velocity, but it is expected to be much higher than in the fixed-bed catalytic activity measurements discussed above. The time-resolved spectra are shown in Figure 10a, d,

DOI: 10.1021/acscatal.5b02480
ACS Catal. 2016, 6, 2163−2177

and g. The spectra of SSZ-13-R are dominated by a band around 400 nm, which is due to polymethylated benzenes.[14,62] For the SSZ-13-F and SSZ-13-F-M25 samples, the spectra initially show the appearance of the band at 400 nm followed by the appearance of additional absorption bands at higher wavelengths, which can be ascribed to bulkier multiring aromatics. For each catalyst sample, the spectra were deconvoluted into two main spectral features by non-negative matrix factorization analysis.[63] These two spectral features are shown in Figure 10b, e, and h. The first component spectrum has a prominent feature at ~400 nm, which relates to polymethylated benzenes.[64−67] The other component spectra are dominated by higher wavelength features, representing methylated naphthalenes as well as methylated multiring aromatics.[62] The contribution of these two components to the visible spectra recorded during the MTO reaction is shown in Figure 10c, f, and i. For SSZ-13-R, the intensity of polymethylated benzenes reaches a maximum with time on stream, and multiring aromatics form at a later time. The amount of these multiring aromatics is relatively low, and their contribution decreases with increasing time on stream. SSZ-13-F and SSZ-13-F-M25 behave quite differently. For both zeolites, it is seen that initially polymethylated benzenes are formed, but that their contribution decreases once larger aromatics are formed. The polymethylated benzenes appeared much earlier in SSZ-13-F-M25 than in SSZ-13-R and SSZ-13-F. This indicates that the enhanced diffusion of methanol through the zeolite crystals due to the presence of mesopores results in more rapid buildup of the hydrocarbon pool species. It can be related to the faster uptake of methanol in the mesoporous SSZ-13 samples compared with the other two microporous samples seen in Figure 8a. Strikingly, the amount of multiring aromatics in SSZ-13-F and SSZ-13-F-M25 was seen to increase for a much longer time than for SSZ-13-R. All of this is consistent with the much larger amount of methanol converted for SSZ-13-F and SSZ-13-F-M25 in the catalytic activity measurements.

In the confocal fluorescence microscopy measurements (Figure 11), three lasers with excitation lines at 488, 561, and 635 nm were used to record images in the middle plane of single spent catalyst crystals. Longer excitation wavelength of the laser is able to visualize larger aromatic species.[62,67] The 2D fluorescence image of a spent SSZ-13-R crystal (Figure 11a, d, and g) shows that the aromatic species are preferentially deposited in the outer regions of the zeolite crystal. The absence of fluorescence originating from the inner regions of the crystal implies that no aromatics were formed. Accordingly, we infer that these regions have rapidly become inaccessible during the initial stages of the MTO reaction. Close inspection of the images shows that multiring aromatics are only formed close to the surface in a relatively thin layer. Naphthalenes and polymethylated benzenes are also formed deeper in the crystal. In stark contrast with this result, the fluorescent images of a spent SSZ-13-F crystal (Figure 11b, e, and h) show that the aromatic species are homogeneously distributed throughout the crystal. These data show that a much larger fraction of the micropore space of SSZ-13-F has been utilized in the MTO reaction. For spent SSZ-13-F-M25 (Figure 11c, f, and i), the images recorded upon excitation at 561 and 635 nm are very similar to those of SSZ-13-F in the sense that the whole crystal contains methylated polyaromatics. A significant difference, however, is the much lower amount of polymethylated naphthalenes (visualized by 488 nm laser). This indicates that the polymethylated naphthalenes have already been converted into bulkier multiring aromatics. It points to a much higher reaction rate in the mesoporous sample. We link this to the faster transport of methanol inside the zeolite crystals. In several images of SSZ-13-F-M25, one observes smaller and sometimes larger patches without fluorescence in all three images, which may be due to the presence of larger pores.

The most salient finding of the confocal fluorescence microscopy study is that the crystals of SSZ-13-F and SSZ-13-F-M25 are much better utilized during the MTO reaction than the SSZ-13-R crystals. This qualitatively corresponds with the differences in catalytic performance in the MTO reaction. In reaction engineering terms, the effectiveness factor of the SSZ-13-R crystals for the MTO reaction is lower than that of the SSZ-13-F and SSZ-13-F-M*x* crystals.[68] The spatially resolved data indicate that, in SSZ-13-R, the micropores become rapidly blocked by multiring aromatics during the initial stages of the reaction. It suggests that the MTO reaction in SSZ-13-R is limited to a relatively small fraction of the zeolite crystal. These large carbonaceous deposits are mainly formed close to the external surface. Once multiring aromatics are formed, the zeolite crystals become inaccessible to methanol and the reaction stops. These gradients over the zeolite crystal disappear when the SSZ-13 zeolite contains additional porosity due to the effect of NaF and mesopores. The data also show that the reaction rate for the mesoporous sample is much higher with the consequence that at the time scale of the in situ experiment nearly all polymethylated benzenes have been converted to larger aromatic species.

CONCLUSIONS

A set of highly crystalline hierarchical SSZ-13 zeolites was successfully synthesized in the presence of $C_{22-4-4}{\cdot}Br_2$ and fluoride anions. A manifold of characterization techniques has been applied to determine the structural, textural, and acidic properties of the samples. The set of thus-prepared zeolites have comparable Si/Al ratios, Brønsted acid site densities, and intrinsic acid strength of these acid sites. With the addition of fluoride anions and a diquaternary ammonium surfactant mesoporogen to the synthesis mixture, the SSZ-13 zeolites exhibit trimodal porosity comprising native CHA micropores, micropores with sizes slightly larger than the CHA micropores, and mesopores. These hierarchical zeolites showed substantially improved mass transport inside the crystals and deactivated at a lower rate in the MTO reaction as compared with bulk SSZ-13. Confocal fluorescence microscopy revealed that aromatic species including multiring aromatics that cause deactivation are homogeneously deposited throughout the crystals of such hierarchical SSZ-13 zeolites. SSZ-13 hierarchization resulted in complete utilization of the micropore space. As such, these improved SSZ-13 zeolites may find application in commercial MTO operations. A challenge to be overcome is the high cost of the TMAdaOH template for SSZ-13 synthesis as compared with the cheap structure-directing agents used to obtain SAPO-34 (Table S2).

ASSOCIATED CONTENT

Supporting Information

The Supporting Information is available free of charge on the ACS Publications website at DOI: 10.1021/acscatal.5b02480.

Detailed information regarding XRD, ^{1}H MAS NMR, ^{27}Al 3QMAS NMR, ^{19}F MAS NMR, FTIR spectra of

DOI: 10.1021/acscatal.5b02480
ACS Catal. 2016, 6, 2163−2177

absorbed propylene, total methanol conversion capacity of the samples, and regeneration stability test (PDF)

AUTHOR INFORMATION

Corresponding Author

*E-mail: e.j.m.hensen@tue.nl.

Notes

The authors declare no competing financial interest.

ACKNOWLEDGMENTS

The authors acknowledge financial support from the Technology Foundation (STW) of The Netherlands Organization for Scientific Research (NWO) (E.J.M.H.), the China Scholarship Council (X.Z.), and NWO−CW (VENI grant, J.R.M.; TOP research grant, B.M.W.). We thank J. J. G. van Velzen, A. M. Elemans-Mehring, and F. Meirer for SEM, ICP-OES, and in situ visible light spectra data analyses.

REFERENCES

(1) Laurendeau, N. M. *Prog. Energy Combust. Sci.* **1978**, *4*, 221−270.
(2) Hickman, D. A.; Schmidt, L. D. *Science* **1993**, *259*, 343−346.
(3) Asadullah, M.; Ito, S.; Kunimori, K.; Yamada, M.; Tomishige, K. *J. Catal.* **2002**, *208*, 255−259.
(4) Haw, J. F.; Song, W.; Marcus, D. M.; Nicholas, J. B. *Acc. Chem. Res.* **2003**, *36*, 317−326.
(5) Wang, W.; Hunger, M. *Acc. Chem. Res.* **2008**, *41*, 895−904.
(6) Xu, S.; Zheng, A.; Wei, Y.; Chen, J.; Li, J.; Chu, Y.; Zhang, M.; Wang, Q.; Zhou, Y.; Wang, J.; Deng, F.; Liu, Z. *Angew. Chem.* **2013**, *125*, 11778−11782.
(7) Galadima, A.; Muraza, O. *Ind. Eng. Chem. Res.* **2015**, *54*, 4891−4905.
(8) Dahl, I. M.; Kolboe, S. *J. Catal.* **1994**, *149*, 458−464.
(9) Dahl, I. M.; Kolboe, S. *J. Catal.* **1996**, *161*, 304−309.
(10) Olsbye, U.; Svelle, S.; Bjørgen, M.; Beato, P.; Janssens, T. V. W.; Joensen, F.; Bordiga, S.; Lillerud, K. P. *Angew. Chem., Int. Ed.* **2012**, *51*, 5810−5831.
(11) Park, J. W.; Lee, J. Y.; Kim, K. S.; Hong, S. B.; Seo, G. *Appl. Catal., A* **2008**, *339*, 36−44.
(12) Bleken, F.; Bjørgen, M.; Palumbo, L.; Bordiga, S.; Svelle, S.; Lillerud, K. P.; Olsbye, U. *Top. Catal.* **2009**, *52*, 218−228.
(13) Sommer, L.; Mores, D.; Svelle, S.; Stöcker, M.; Weckhuysen, B. M.; Olsbye, U. *Microporous Mesoporous Mater.* **2010**, *132*, 384−394.
(14) Mores, D.; Stavitski, E.; Kox, M. H. F.; Kornatowski, J.; Olsbye, U.; Weckhuysen, B. M. *Chem. - Eur. J.* **2008**, *14*, 11320−11327.
(15) Bibby, D. M.; Howe, R. F.; McLellan, G. D. *Appl. Catal., A* **1992**, *93*, 1−34.
(16) Stöcker, M. *Microporous Mesoporous Mater.* **1999**, *29*, 3−48.
(17) Aramburo, L. R.; Ruiz-Martínez, J.; Sommer, L.; Arstad, B.; Buitrago-Sierra, R.; Sepúlveda-Escribano, A.; Zandbergen, H. W.; Olsbye, U.; de Groot, F. M. F.; Weckhuysen, B. M. *ChemCatChem* **2013**, *5*, 1386−1394.
(18) Wu, L.; Degirmenci, V.; Magusin, P. C. M. M.; Szyja, B. M.; Hensen, E. J. M. *Chem. Commun.* **2012**, *48*, 9492−9494.
(19) Wu, L.; Degirmenci, V.; Magusin, P. C. M. M.; Lousberg, N. J. H. G. M.; Hensen, E. J. M. *J. Catal.* **2013**, *298*, 27−40.
(20) Choi, M.; Na, K.; Kim, J.; Sakamoto, Y.; Terasaki, O.; Ryoo, R. *Nature* **2009**, *461*, 246−249.
(21) Corma, A.; Puche, M.; Rey, F.; Sankar, G.; Teat, S. J. *Angew. Chem., Int. Ed.* **2003**, *42*, 1156−1159.
(22) Corma, A.; Díaz-Cabañas, M. J.; Martínez-Triguero, J.; Rey, F.; Rius, J. *Nature* **2002**, *418*, 514−517.
(23) Eilertsen, E. A.; Nilsen, M. H.; Wendelbo, R.; Olsbye, U.; Lillerud, K. P. *Stud. Surf. Sci. Catal.* **2008**, *174*, 265−268.
(24) Barrett, P. A.; Camblor, M. A.; Corma, A.; Jones, R. H.; Villaescusa, L. A. *J. Phys. Chem. B* **1998**, *102*, 4147−4155.
(25) Larlus, O.; Valtchev, V. P. *Chem. Mater.* **2005**, *17*, 881−886.
(26) Cantín, Á.; Corma, A.; Díaz-Cabañas, M. J.; Jordá, J. L.; Moliner, M.; Rey, F. *Angew. Chem., Int. Ed.* **2006**, *45*, 8013−8015.
(27) Corma, A.; Moliner, M.; Cantín, Á.; Díaz-Cabañas, M. J.; Jordá, J. L.; Zhang, D.; Sun, J.; Jansson, K.; Hovmöller, S.; Zou, X. *Chem. Mater.* **2008**, *20*, 3218−3223.
(28) Zhu, X.; Kosinov, N.; Hofmann, J. P.; Mezari, B.; Qian, Q.; Rohling, R.; Weckhuysen, B. M.; Ruiz-Martínez, J.; Hensen, E. J. M. *Chem. Commun.* **2016**, *52*, 3227.
(29) Massiot, D.; Fayon, F.; Capron, M.; King, I.; Le Calvé, S.; Alonso, B.; Durand, J.; Bujoli, B.; Gan, Z.; Hoatson, G. *Magn. Reson. Chem.* **2002**, *40*, 70−76.
(30) Kobayashi, Y.; Li, Y.; Wang, Y.; Wang, D. *Chin. J. Catal.* **2013**, *34*, 2192−2199.
(31) Ji, Y.; Deimund, M. A.; Bhawe, Y.; Davis, M. E. *ACS Catal.* **2015**, *5*, 4456−4465.
(32) Barrett, P. A.; Camblor, M. A.; Corma, A.; Jones, R. H.; Villaescusa, L. A. *J. Phys. Chem. B* **1998**, *102*, 4147−4155.
(33) *Zeolites and Catalysis* Cejka, J., Corma, A., Zones, S. I., Eds.; Wiley, 2010.
(34) Shi, J.; Anderson, M. W.; Carr, S. W. *Chem. Mater.* **1996**, *8*, 369−375.
(35) Engelhardt, G.; Lohse, U.; Lippmaa, E.; Tarmak, M.; Mägi, M. *Z. Anorg. Allg. Chem.* **1981**, *482*, 49−64.
(36) Eilertsen, E. A.; Arstad, B.; Svelle, S.; Lillerud, K. P. *Microporous Mesoporous Mater.* **2012**, *153*, 94−99.
(37) Hunger, M.; Ernst, S.; Steuernagel, S.; Weitkamp, J. *Microporous Mater.* **1996**, *6*, 349−353.
(38) Hunger, M.; Kärger, J.; Pfeifer, H.; Caro, J.; Zibrowius, B.; Bülow, M.; Mostowicz, R. *J. Chem. Soc., Faraday Trans. 1* **1987**, *83*, 3459−3468.
(39) Hunger, M.; Anderson, M. W.; Ojo, A.; Pfeifer, H. *Microporous Mater.* **1993**, *1*, 17−32.
(40) Trébosc, J.; Wiench, J. W.; Huh, S.; Lin, V. S. Y.; Pruski, M. *J. Am. Chem. Soc.* **2005**, *127*, 3057−3068.
(41) Huo, H.; Peng, L.; Gan, Z.; Grey, C. P. *J. Am. Chem. Soc.* **2012**, *134*, 9708−9720.
(42) Gabrienko, A. A.; Danilova, I. G.; Arzumanov, S. S.; Toktarev, A. V.; Freude, D.; Stepanov, A. G. *Microporous Mesoporous Mater.* **2010**, *131*, 210−216.
(43) Deng, F.; Yue, Y.; Ye, C. *J. Phys. Chem. B* **1998**, *102*, 5252−5256.
(44) Van Eck, E. R. H.; Janssen, R.; Maas, W. E. J. R.; Veeman, W. S. *Chem. Phys. Lett.* **1990**, *174*, 428−432.
(45) Bordiga, S.; Regli, L.; Cocina, D.; Lamberti, C.; Bjørgen, M.; Lillerud, K. P. *J. Phys. Chem. B* **2005**, *109*, 2779−2784.
(46) Smith, L. J.; Davidson, A.; Cheetham, A. K. *Catal. Lett.* **1997**, *49*, 143−146.
(47) Emeis, C. A. *J. Catal.* **1993**, *141*, 347−354.
(48) Camblor, M. A.; Villaescusa, L. A.; Diaz-Cabanas, M. J. *Top. Catal.* **1999**, *9*, 59−76.
(49) Möller, K.; Bein, T. *Chem. Soc. Rev.* **2013**, *42*, 3689−3707.
(50) Buurmans, I. L. C.; Ruiz-Martínez, J.; Knowles, W. V.; van der Beek, D.; Bergwerff, J. A.; Vogt, E. T. C.; Weckhuysen, B. M. *Nat. Chem.* **2011**, *3*, 862−867.
(51) Buurmans, I. L. C.; Ruiz-Martínez, J.; van Leeuwen, S. L.; van der Beek, D.; Bergwerff, J. A.; Knowles, W. V.; Vogt, E. T. C.; Weckhuysen, B. M. *Chem. - Eur. J.* **2012**, *18*, 1094−1101.
(52) Dai, W.; Wang, X.; Wu, G.; Guan, N.; Hunger, M.; Li, L. *ACS Catal.* **2011**, *1*, 292−299.
(53) Remy, T.; Cousin Saint Remi, J.; Singh, R.; Webley, P. A.; Baron, G. V.; Denayer, J. F. M. *J. Phys. Chem. C* **2011**, *115*, 8117−8125.
(54) Ghosh, A. K.; Kydd, R. A. *J. Catal.* **1986**, *100*, 185−195.
(55) Wilson, S.; Barger, P. *Microporous Mesoporous Mater.* **1999**, *29*, 117−126.
(56) Tian, P.; Wei, Y.; Ye, M.; Liu, Z. *ACS Catal.* **2015**, *5*, 1922−1938.
(57) Chen, D.; Rebo, H. P.; Moljord, K.; Holmen, A. *Ind. Eng. Chem. Res.* **1997**, *36*, 3473−3479.

DOI: 10.1021/acscatal.5b02480
ACS Catal. 2016, 6, 2163−2177

(58) Li, J.; Qi, Y.; Liu, Z.; Liu, G.; Chang, F. *Chin. J. Catal.* **2008**, *29*, 660−664.
(59) Li, J.; Qi, Y.; Liu, Z.; Liu, G.; Zhang, D. *Catal. Lett.* **2008**, *121*, 303−310.
(60) Sun, Q.; Wang, N.; Xi, D.; Yang, M.; Yu, J. *Chem. Commun.* **2014**, *50*, 6502−6505.
(61) Bjørgen, M.; Joensen, F.; Spangsberg Holm, M.; Olsbye, U.; Lillerud, K. P.; Svelle, S. *Appl. Catal., A* **2008**, *345*, 43−50.
(62) Van Speybroeck, V.; Hemelsoet, K.; De Wispelaere, K.; Qian, Q.; Van der Mynsbrugge, J.; De Sterck, B.; Weckhuysen, B. M.; Waroquier, M. *ChemCatChem* **2013**, *5*, 173−184.
(63) Borodina, E.; Meirer, F.; Lezcano-González, I.; Mokhtar, M.; Asiri, A. M.; Al-Thabaiti, S. A.; Basahel, S. N.; Ruiz-Martinez, J.; Weckhuysen, B. M. *ACS Catal.* **2015**, *5*, 992−1003.
(64) Mores, D.; Kornatowski, J.; Olsbye, U.; Weckhuysen, B. M. *Chem. - Eur. J.* **2011**, *17*, 2874−2884.
(65) Palumbo, L.; Bonino, F.; Beato, P.; Bjørgen, M.; Zecchina, A.; Bordiga, S. *J. Phys. Chem. C* **2008**, *112*, 9710−9716.
(66) Hemelsoet, K.; Qian, Q.; De Meyer, T.; De Wispelaere, K.; De Sterck, B.; Weckhuysen, B. M.; Waroquier, M.; Van Speybroeck, V. *Chem. - Eur. J.* **2013**, *19*, 16595−16606.
(67) Qian, Q.; Ruiz-Martínez, J.; Mokhtar, M.; Asiri, A. M.; Al-Thabaiti, S. A.; Basahel, S. N.; van der Bij, H. E.; Kornatowski, J.; Weckhuysen, B. M. *Chem. - Eur. J.* **2013**, *19*, 11204−11215.
(68) Weisz, P. B.; Hicks, J. S. *Chem. Eng. Sci.* **1962**, *17*, 265−275.

DOI: 10.1021/acscatal.5b02480
ACS Catal. 2016, 6, 2163−2177